International Journal of
*Molecular Sciences*

MDPI

*Article*

# Gas-Sensing Performance of Metal Oxide Heterojunction Materials for $SF_6$ Decomposition Gases: A DFT Study

**Tingting Zeng [1], Donglin Ma [1] and Yingang Gui [2,*]**

[1] College of Physics and Engineering, Chengdu Normal University, Chengdu 611130, China; 073022@cdnu.edu.cn (T.Z.); 073018@cdnu.edu.cn (D.M.)
[2] College of Engineering and Technology, Southwest University, Chongqing 400715, China
* Correspondence: yinganggui@swu.edu.cn

**Abstract:** The online monitoring of GIS equipment can be realized through detecting $SF_6$ decomposition gasses. Metal oxide heterojunctions are widely used as gas-sensing materials. In this study, the structural and electrical properties of $In_2O_3$-ZnO and $TiO_2$-ZnO heterojunctions were analyzed based on density functional theory calculations. After heterojunction structural optimization, the electrical conductivity of these two heterojunctions was enhanced compared to each intrinsic model, and the electrical conductivity is ranked as follows: $In_2O_3$-ZnO heterojunction > $TiO_2$-ZnO heterojunction. The gas-sensing response of these two heterojunctions to four $SF_6$ decomposition gasses, $H_2S$, $SO_2$, $SOF_2$, and $SO_2F_2$, was investigated. For gas adsorption systems, the adsorption energy, charge transfer, density of states, charge difference density, and frontier molecular orbitals were calculated to analyze the adsorption and gas-sensing performance. For gas adsorption on the $In_2O_3$-ZnO heterojunction surface, the induced conductivity changes are in the following order: $H_2S$ > $SO_2F_2$ > $SOF_2$ > $SO_2$. For gas adsorption on the $TiO_2$-ZnO heterojunction surface, $H_2S$ and $SOF_2$ increase conductivity, and $SO_2$ and $SO_2F_2$ decrease conductivity.

**Keywords:** $SF_6$ decomposition gasses; metal oxide heterojunction; gas-sensing properties; DFT calculation

check for updates

**Citation:** Zeng, T.; Ma, D.; Gui, Y. Gas-Sensing Performance of Metal Oxide Heterojunction Materials for $SF_6$ Decomposition Gases: A DFT Study. *Int. J. Mol. Sci.* **2024**, *25*, 8009. https://doi.org/10.3390/ijms25158009

Academic Editors: Paolo Prosposito and Luca Burratti

Received: 28 May 2024
Revised: 18 July 2024
Accepted: 19 July 2024
Published: 23 July 2024

**Copyright:** © 2024 by the authors. Licensee MDPI, Basel, Switzerland. This article is an open access article distributed under the terms and conditions of the Creative Commons Attribution (CC BY) license (https://creativecommons.org/licenses/by/4.0/).

## 1. Introduction

In modern power systems, the gas insulated switchgear (GIS) is an essential critical piece of equipment to ensure the safe and stable operation of the power grid [1]. Sulfur hexafluoride gas ($SF_6$) is widely used in GIS equipment due to its excellent insulation and arc extinguishing performance [2]. However, during the long-term operation of GIS equipment, external environmental factors (such as overvoltage and high temperature) and inherent insulation defects of the equipment itself may lead to internal discharge and overheating faults [3]; furthermore, this can lead to $SF_6$ decomposition, which has a serious impact on GIS reliability. Therefore, in order to ensure the stable operation of GIS equipment, effective online monitoring measures must be taken to quickly identify and eliminate the potential insulation faults [4]. Research has confirmed that $SF_6$ decomposition gasses mainly include $H_2S$, $SO_2$, $SOF_2$, and $SO_2F_2$, and the operating state of the GIS device can be reflected by detecting the presence and concentration of these gasses [5,6]. Therefore, it is necessary to explore gas-sensitive materials with high sensitivity and selectivity for $SF_6$ decomposition gasses detection.

In recent years, the adsorption research on $SF_6$ decomposition gas mainly focuses on graphene, two-dimensional metal sulfur compounds (TMDCs), metal oxides, and surface-modified metal oxides [7–9]. Among them, metal oxides are widely used materials with the characteristics of low cost, low power consumption, and easy synthesis for gas detection [10], including ZnO, $TiO_2$, $In_2O_3$, $SnO_2$, and $WO_3$. ZnO is an n-type semiconductor, which is widely used for detecting toxic and hazardous gasses due to its wide bandgap and high electron mobility [11]. At the same time, researchers have also proposed various

forms of nanostructures, such as nanosheets [12], nanorings [13], nanowires [14], and nanorods [15], to improve the sensitivity, selectivity, and stability of the ZnO-based gas sensor, and to reduce the working temperature and reaction recovery time. Razavi et al. prepared ZnO@$TiO_2$ nanocomposites and verified their potential in the determination of hydrazine ($N_2H_4$) [16]. The research showed that $TiO_2$ exhibits high selectivity and sensitivity towards small gas molecules [17–19]. Shooshtariet al. prepared an electronic nose based on carbon nanotube-titanium dioxide hybrid nanostructures for the detection and discrimination of volatile organic compounds (VOCs) [20]. In addition, $In_2O_3$ is also widely used in gas detection and monitoring due to its suitable bandgap and good chemical stability, and excellent gas-sensing performance [21,22]. The gas-sensing property of $In_2O_3$ can also be improved through surface metal modification or the formation of heterojunctions [23]. However, intrinsic metal oxides have limited gas sensitivity to specific gasses, and metal oxide heterojunctions are often used to improve the gas sensitivity of metal oxides-based gas sensors due to Fermi level effects and synergistic effects between different metal oxides [24,25]. Cheng et al. reported an ammonia sensor based on the ZnO/CuO heterojunction using a hydrothermal method, which effectively improved the gas-sensing property of the ZnO sensor for $NH_3$ at room temperature [26].

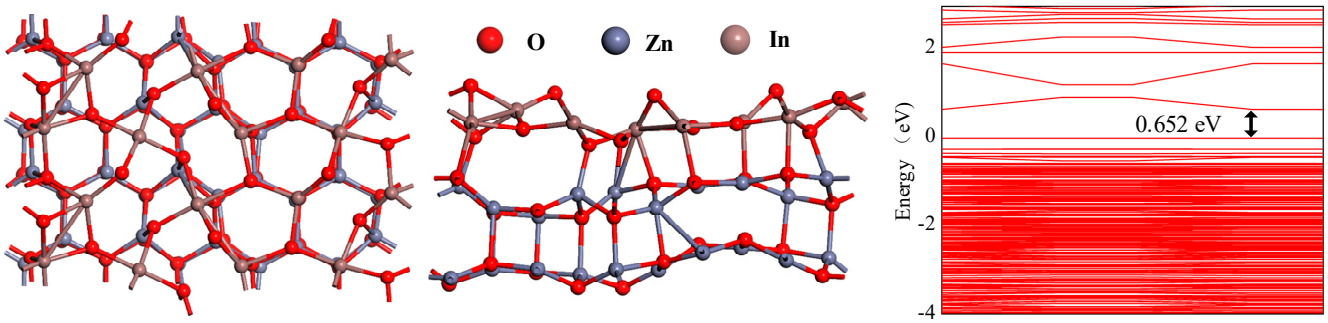
In order to improve the sensitivity and selectivity of gas-sensitive materials towards the $SF_6$ decomposition gasses of $H_2S$, $SO_2$, $SOF_2$, and $SO_2F_2$, this study adopts $In_2O_3$-ZnO and $TiO_2$-ZnO heterojunctions as gas-sensitive materials, and studies their gas-sensing properties to $SF_6$ decomposition gasses based on density functional theory (DFT). Firstly, the structural models of $In_2O_3$-ZnO and $TiO_2$-ZnO heterojunctions were constructed and optimized, and then the structural and energy band properties were analyzed. Secondly, the adsorption structures of different $SF_6$ decomposition gasses on the heterojunction surface were constructed and optimized. Finally, by analyzing the density of states (DOS) and charge difference density (CDD) of gas adsorption systems, the adsorption performance of the metal oxide heterojunction materials for $SF_6$ decomposition gasses was analyzed. The research results play an important role in promoting the application of gas-sensing technology in the online monitoring of power insulation equipment.

## 2. Results and Discussion

### *2.1. Adsorption Properties of $In_2O_3$-ZnO Heterojunction on $SF_6$ Decomposition Gases*

#### 2.1.1. Construction and Energy Band Analysis of $In_2O_3$-ZnO Heterojunction Model

In the section, the most stable structure of the $In_2O_3$-ZnO heterojunction model was constructed and optimized, as shown in Figure 1a,b. The $In_2O_3$-ZnO heterojunction contains a total of 120 atoms, including 40 atoms in the $In_2O_3$ layer and 80 atoms in the ZnO heterojunction layer. The ZnO heterojunction crystal plane is placed in the lower layer, and the $In_2O_3$ crystal plane is placed in the upper layer. The lattice parameters of the ZnO heterojunction are as follows: a = 11.2558 Å, b = 16.2464 Å, and $\gamma = 90^o$. The lattice parameters of $In_2O_3$ are as follows: a = 11.0324 Å, b = 16.0283 Å, and $\gamma = 90^o$. The lattice parameters of the constructed $In_2O_3$-ZnO heterojunction are as follows: a = 11.1441 Å, b = 16.1373 Å, and $\gamma = 90^o$. In heterostructures, there is a formation of chemical bonds between the $In_2O_3$ layer and the ZnO layer, which implies a strong interaction force between the two metal oxides. In addition, its enormous formation energy (−18.017 eV) and significant geometric deformation also prove that the formation between the two materials is highly stable. The energy band structure of the $In_2O_3$-ZnO heterojunction shown in Figure 1c intuitively displays the electron property of the heterojunction. According to the calculation results, the energy required for electrons to transition from the valence band to the conduction band is 0.652 eV. Compared to the intrinsic $In_2O_3$ (1.538 eV) and intrinsic ZnO heterojunction (1.769 eV), the significant decrease in energy indicates that the conductivity of the heterojunction is superior.




(a) $In_2O_3$-ZnO (Top view) (b) $In_2O_3$-ZnO (Side view) (c) Energy band

**Figure 1.** (**a**,**b**) The structure of $In_2O_3$-ZnO heterojunction, (**c**) the band structure of $In_2O_3$-ZnO heterojunction.

2.1.2. Adsorption Properties of $In_2O_3$-ZnO Heterojunction

- Gas adsorption structure analysis

Figure 2 shows the most stable adsorption structures for $H_2S$, $SO_2$, $SOF_2$, and $SO_2F_2$ on the $In_2O_3$-ZnO heterojunction surface, and Table 1 lists the corresponding adsorption parameters. For the $H_2S$ adsorption system shown in Figure 2(a1,a2), the strong binding force between the O and H atoms leads to the breaking of the H-S bond, resulting in the formation of a new H-O bond (1.008 Å); here, a new chemical bond is formed between the S atom and the nearest In atom with a length of 2.486 Å. As listed in Table 1, the adsorption energy of the $H_2S$ adsorption system reaches −1.924 eV, indicating chemical adsorption. $H_2S$ molecules act as electron contributors and transfer the 0.255 $|e|$ charge to the $In_2O_3$-ZnO heterojunction, which is consistent with the reducibility properties of $H_2S$. As shown in Figure 2(b1,b2), the O atoms of the $SO_2$ molecule form chemical bonds with In atoms, while the S atom of the $SO_2$ molecule forms chemical bonds with O atoms, resulting in varying degrees of elongation of the S-O bond in $SO_2$. Meanwhile, the system has an adsorption energy of −1.992 eV and a charge transfer capacity of −0.361 $|e|$, indicating a strong binding force between the $SO_2$ molecules and the $In_2O_3$-ZnO heterojunction. For the adsorption systems of $SOF_2$ and $SO_2F_2$, shown in Figure 2(c1,c2,d1,d2), there is a significant distance between the gas molecules and heterojunctions; gas molecules can easily desorb from the surface of the $In_2O_3$-ZnO heterojunction, indicating that the adsorption process is physical adsorption. In addition, the small adsorption energy ($SOF_2$: $E_{ads}$ = −0.465 eV, $SO_2F_2$: $E_{ads}$ = −0.501 eV) and the small amount of charge transfer ($SOF_2$: $Q_t$ = 0.016 $|e|$, $SO_2F_2$: $Q_t$ = 0.011 $|e|$) also confirm this physical adsorption effect. In summary, the adsorption process of $H_2S$ and $SO_2$ is chemical adsorption, and the molecular structure of the $H_2S$ gas molecules is destroyed, making it difficult to carry out the desorption process. The adsorption process of $SOF_2$ and $SO_2F_2$ is physical adsorption and the adsorption energy is moderate, which together can have a certain adsorption capacity for gas molecules and make desorption possible.

**Table 1.** The adsorption parameters of $H_2S$, $SO_2$, $SOF_2$, and $SO_2F_2$ on $In_2O_3$-ZnO heterojunction surface.

| System | Distance (Å) | $E_{ads}$ (eV) | $Q_t$ (*e*) |
|---|---|---|---|
| $H_2S/In_2O_3$-ZnO | In-S:2.486<br>H-O:1.008 | −1.924 | 0.255 |
| $SO_2/In_2O_3$-ZnO | In-O:2.190<br>S-O:1.561 | −1.992 | −0.361 |
| $SOF_2/In_2O_3$-ZnO | In-S:3.687 | −0.465 | 0.016 |
| $SO_2F_2/In_2O_3$-ZnO | In-S:3.902 | −0.501 | 0.011 |

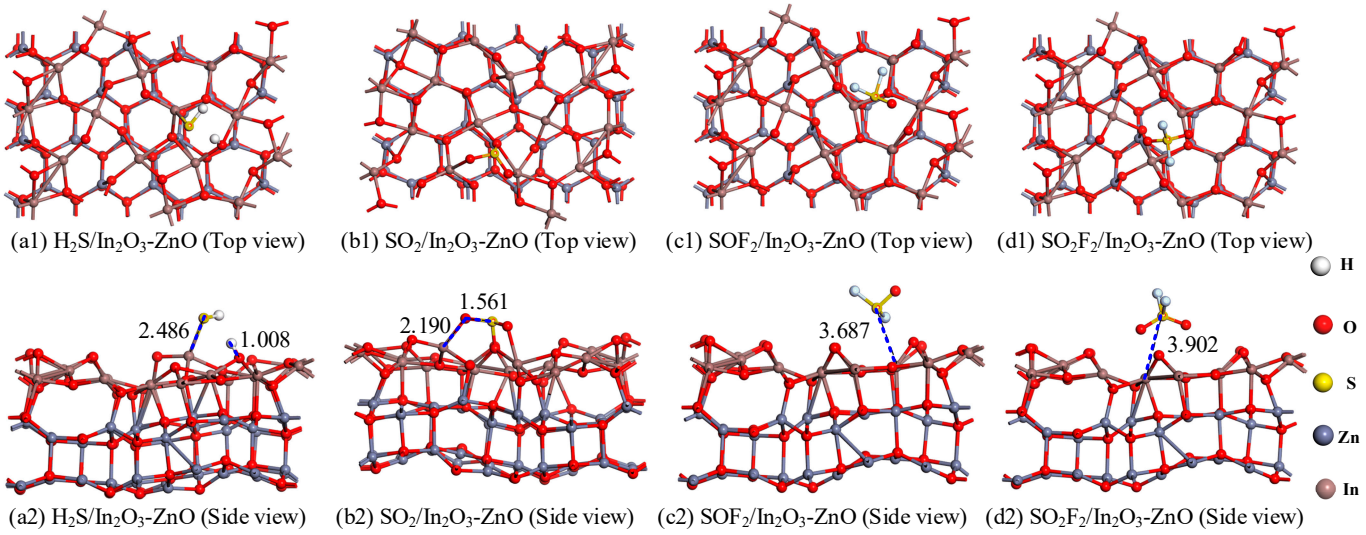



**Figure 2.** The gasses adsorption structures of (**a1**,**a2**) $H_2S$, (**b1**,**b2**) $SO_2$, (**c1**,**c2**) $SOF_2$, and (**d1**,**d2**) $SO_2F_2$ on $In_2O_3$-ZnO heterojunction.

- DOS, CDD, and molecular orbital analysis

Figure 3 shows the density of states distribution of $H_2S$, $SO_2$, $SOF_2$, and $SO_2F_2$ adsorption on the $In_2O_3$-ZnO heterojunction surface. In the $H_2S$ adsorption system shown in Figure 3(a1,a2), there is no significant change in TDOS. It can also be observed from PDOS that the hybridization phenomenon between atomic orbitals is very weak. This phenomenon indicates that the conductivity of the system remains almost unchanged before and after $H_2S$ adsorption. Figure 3(b1,b2) shows the TDOS and PDOS of the $SO_2$ gas adsorption system. It can be observed that TDOS almost completely overlaps above the Fermi level. However, the overall density of states shows an increasing trend below the Fermi level, with the peak value increasing most significantly around $-5$ eV. Due to the increase in electron filling probability at this location, the conductivity of the system increases. In the PDOS distribution, there is a very obvious hybridization phenomenon between the 5p orbitals of the In atoms and the 2p orbitals of the S atoms between $-10$ eV and 5 eV. This phenomenon confirms the strong chemical interaction between the $SO_2$ and $In_2O_3$-ZnO heterojunction, as well as the increase in TDOS near $-5$ eV. During the adsorption process of $SOF_2$ shown in Figure 3(c1,c2), TDOS remains almost unchanged, which is consistent with its small adsorption energy and small charge transfer performance. In Figure 3(d1,d2), TDOS also keeps overlapping before and after the adsorption of $SO_2F_2$ gas, except in two new small peaks, which appear near $-10$ eV. In the PDOS analysis of the $SO_2F_2$ adsorption process, only In-5s orbitals and F-2p orbitals have a certain degree of hybridization, but the hybridization is not significant, which has a certain impact on improving gas adsorption performance. This result explains that compared to $SOF_2$ gas molecules, the $SO_2F_2$ gas adsorption system has a greater adsorption energy.

To further understand the adsorption mechanism of the $In_2O_3$-ZnO heterojunction on the four $SF_6$ decomposition gasses, the charge difference density before and after adsorption were studied as shown in Figure 4; the increase in charge density is shown in red, while the decrease is shown in blue. For the $SOF_2$ and $SO_2F_2$ gas molecules adsorption, there is almost no charge transfer between the $In_2O_3$-ZnO heterojunction and the gas molecules. When adsorbing $H_2S$ gas molecules, the S atom acts as an electron acceptor, indicating a decrease in the number of charges around the S atom. However, the red color around the S atom is very weak, and the entire $H_2S$ gas molecule transfers 0.255 $|e|$ to the $In_2O_3$-ZnO heterojunction substrate during the adsorption process. When adsorbing $SO_2$ gas molecules, the charge density around the O atom of $SO_2$ molecules significantly increases, indicating that the charge transfers from the $In_2O_3$-ZnO heterojunction to $SO_2$. This is attributed to the formation of chemical bonds between gas molecules and the substrate, as

well as the large adsorption energy. The $In_2O_3$-ZnO heterojunction has a good adsorption effect on the $SO_2$ gas molecule, but this adsorption force is not sufficient to break the original chemical bonds of the $SO_2$ gas molecules. Therefore, the $SO_2$ gas molecules have the potential for desorption.

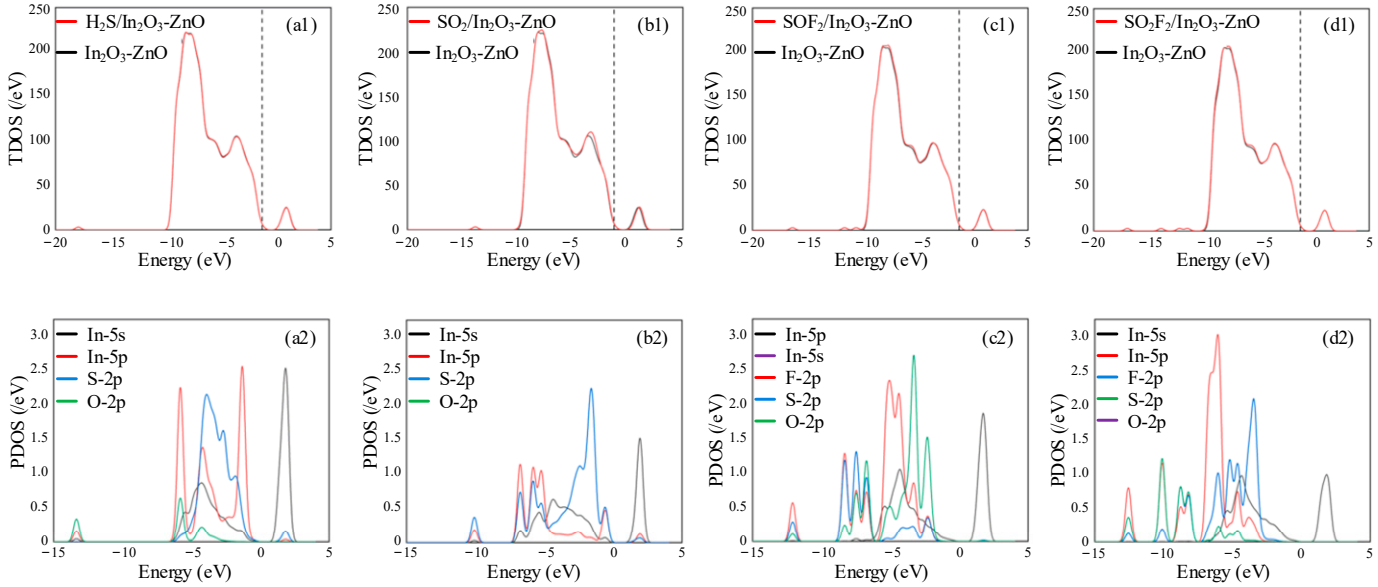



**Figure 3.** The TDOS and PDOS of (**a1**,**a2**) $H_2S$, (**b1**,**b2**) $SO_2$, (**c1**,**c2**) $SOF_2$, and (**d1**,**d2**) $SO_2F_2$ on $In_2O_3$-ZnO heterojunction.

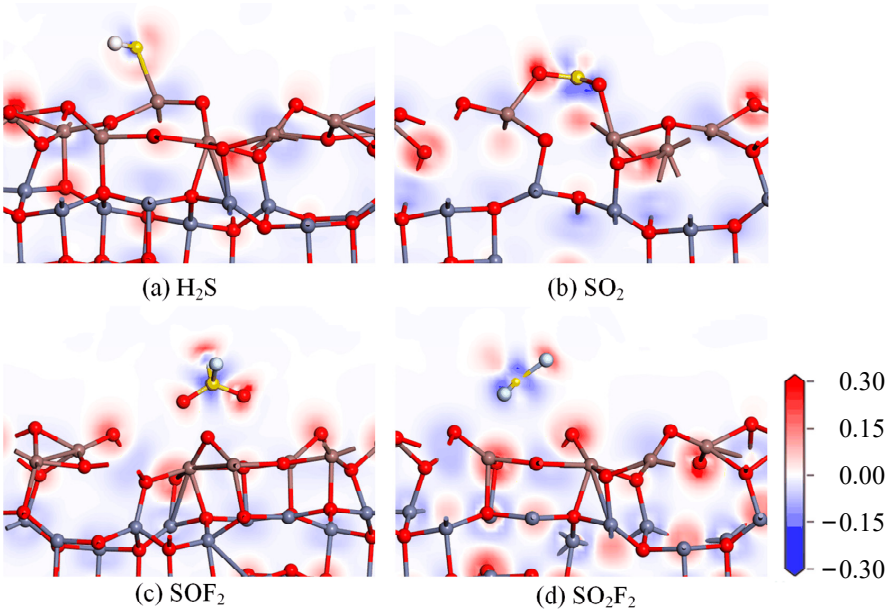



**Figure 4.** The CDD of (**a**) $H_2S$, (**b**) $SO_2$, (**c**) $SOF_2$, and (**d**) $SO_2F_2$ on $In_2O_3$-ZnO heterojunction.

Figure 5 shows the changes in the frontier molecular orbitals of the$In_2O_3$-ZnO heterojunction before and after $H_2S$, $SO_2$, $SOF_2$, and $SO_2F_2$ molecules adsorption, where LUMO and HOMO represent the lowest unoccupied molecular orbitals and the highest occupied molecular orbitals, respectively. It can be observed that after gas molecule adsorption, the molecular orbitals and corresponding energies change. Usually, changes in the energy gap can directly affect conductivity. During the adsorption process of $H_2S$ and $SO_2$, there is a significant change in the energy gap value, which is related to chemical adsorption. Specifically, the conductivity of the $H_2S$ adsorption system increases, while the conductivity of the

$SO_2$ adsorption system decreases. After the adsorption of $SOF_2$ and $SO_2F_2$ gas molecules, the energy gap increases, indicating a decrease in conductivity. Although this change is not very obvious, it is consistent with the previous analysis results. According to the extent of the energy gap change, the conductivity changes caused by gas adsorption are ranked in descending order: $SO_2 > H_2S > SO_2F_2 > SOF_2$.

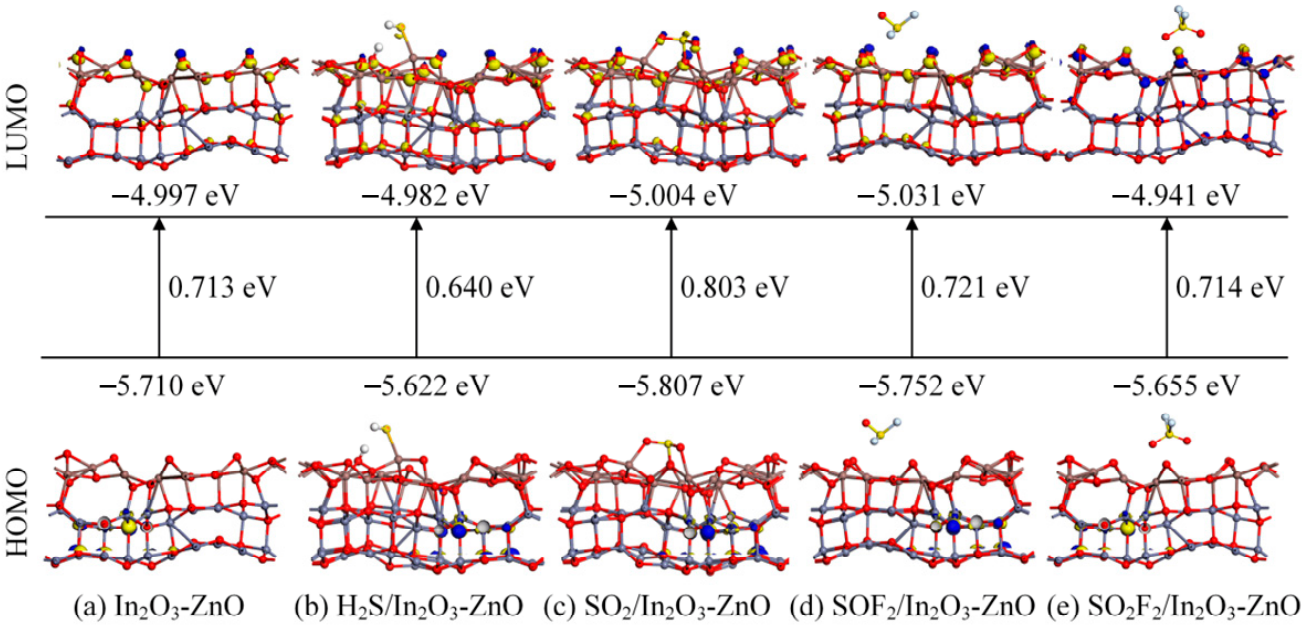



**Figure 5.** Calculated frontier molecular orbitals, HOMO and LUMO, before and after gas adsorption on $In_2O_3$-ZnO heterojunction.

This section calculated and analyzed the adsorption performance of the $In_2O_3$-ZnO heterojunction on four gas molecules: $H_2S$, $SO_2$, $SOF_2$, and $SO_2F_2$. Firstly, the most stable heterostructure and gas adsorption model were structured; each structure has a negative binding or adsorption energy, indicating a spontaneously performed reaction. There is a formation of chemical bonds in the adsorption process of $H_2S$ and $SO_2$, indicating a chemical adsorption, while the adsorption of $SOF_2$ and $SO_2F_2$ belongs to physical adsorption with small adsorption energy and longer adsorption distance. According to the density of states and molecular orbital theory analysis, the conductivity of the $H_2S$ adsorption system increases, while the conductivity of the $SO_2$ adsorption system decreases. However, in the $H_2S$ adsorption system, the structure of gas molecules is disrupted, and cannot be desorbed from the $In_2O_3$-ZnO heterojunction surface. In the $SO_2$ adsorption system, the original chemical bonds of $SO_2$ gas molecules keep intact, showing a certain desorption potential. Therefore, the $In_2O_3$-ZnO heterojunction can serve as an adsorbent material for $H_2S$ gas molecules, while it can also be used as a gas-sensitive material for $SO_2$ gas molecules.

### *2.2. Adsorption Properties of $TiO_2$-ZnO Heterojunction on $SF_6$ Decomposition Gases*

#### 2.2.1. Construction and Energy Band Analysis of $TiO_2$-ZnO Heterojunction Model

This section constructs and optimizes the most stable model by combining the $TiO_2$ and ZnO heterojunction crystal planes. Firstly, the $TiO_2$ crystal plane and ZnO heterojunction crystal plane were constructed and optimized separately. The lattice parameters of the $TiO_2$ crystal were as follows: a = b = 3.776 Å, c = 9.486 Å, $\gamma = 90^o$. The ZnO heterojunction crystal's lattice parameters were as follows: a = b = 3.249 Å, c = 5.205 Å, $\gamma = 90^o$. Then, the $TiO_2$ and ZnO heterojunction crystal planes were cut and expanded, and the obtained parameters were as follows: a = 18.880 Å, b = 10.210 Å, $\gamma = 90^o$ ($TiO_2$ heterojunction); a = 19.496 Å, b = 10.411 Å, $\gamma = 90^o$ (ZnO heterojunction). In this model, the lower layer is the $TiO_2$ layer, and the upper layer is the ZnO heterojunction layer. There are a total of 156 atoms, including 96 atoms in the ZnO layer and 60 atoms in the $TiO_2$ layer. Figure 6a,b shows the

structure of $TiO_2$-ZnO heterojunction after structural optimization, with a binding energy of 12.819 eV. In the model, the $TiO_2$ layer and the ZnO layer are connected by chemical bonds. In addition, the formation of chemical bonds makes it easier for electrons to migrate from the ZnO heterojunction layer to the $TiO_2$ layer, as evidenced by the small energy band (1.292 eV), shown in Figure 6c. Therefore, the conductivity of the $TiO_2$-ZnO heterojunction is enhanced.

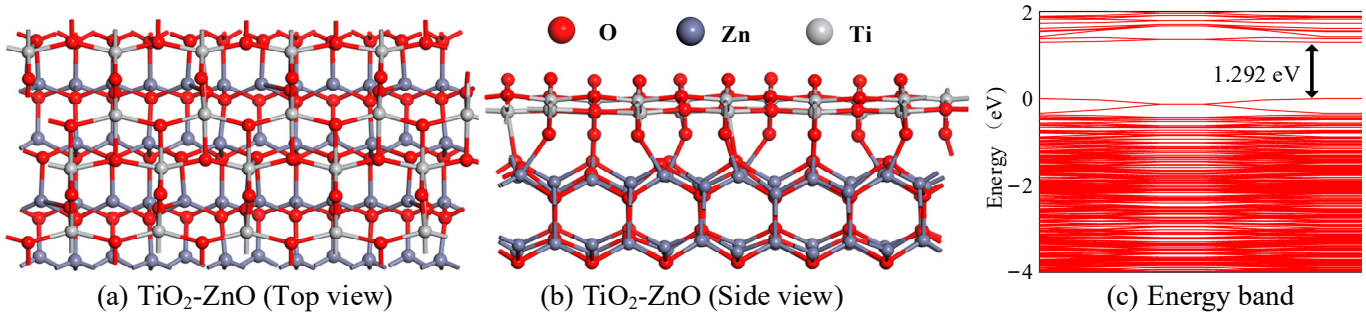



**Figure 6.** (**a**,**b**) The model of $TiO_2$-ZnO heterojunction, (**c**) the band structure of $TiO_2$-ZnO heterojunction.

### 2.2.2. Adsorption Properties of $TiO_2$-ZnO Heterojunction

- Gas adsorption structure analysis

As shown in Figure 7, the most stable adsorption models are calculated by adjusting the various adsorption sites of gas molecules. As listed in Table 2, the $H_2S$ gas adsorption system has the maximum adsorption (−0.788 eV) and the maximum charge transfer amount (0.249 $|e|$). From Figure 7(a1,a2), it can be observed that the shortest distance between the S atoms and Ti atoms is 2.780 Å, and the long adsorption distance makes it impossible to form a chemical bond between the two. In the adsorption system of the $TiO_2$-ZnO heterojunction for the four gasses, only chemical bonds form between the $SO_2$ gas molecule and the substrate material, while the other three gas molecules still maintained a relatively long adsorption distance from the $TiO_2$-ZnO heterojunction substrate. In the adsorption system of $SOF_2$ and $SO_2F_2$, they have a long adsorption distance, small adsorption energy, and a small amount of charge transfer. Therefore, the adsorption of $SOF_2$ and $SO_2F_2$ gas molecules on the $TiO_2$-ZnO heterojunction is physical adsorption. In addition, only the charge transfer amount of the $SO_2$ adsorption system is negative, signifying that gas molecules act as electron acceptors to obtain electrons from the substrate. It is the formation of chemical bonds (S-O: 1.766 Å; Ti-O: 1.958 Å) that facilitate electron migration, allowing $SO_2$ gas molecules to form a whole with the $TiO_2$ layer, and obtain more electrons from the ZnO heterojunction layer. In the other three adsorption systems, the $TiO_2$ layer acts as a stronger electron acceptor, causing gas molecules to lose electrons. In the above gas adsorption, the molecular structure of the gas molecules is not disrupted. Therefore, under certain conditions, the four gas molecules can desorb from the surface of the $TiO_2$-ZnO heterojunction.

**Table 2.** The adsorption parameters of $H_2S$, $SO_2$, $SOF_2$, and $SO_2F_2$ on $TiO_2$-ZnO heterojunction surface.

| System | Distance (Å) | $E_{ads}$ (eV) | $Q_t$ ($e$) |
|---|---|---|---|
| $H_2S/TiO_2$-ZnO | Ti-S:2.780 | −0.788 | 0.249 |
| $SO_2/TiO_2$-ZnO | S-O:1.766<br>Ti-O:1.958 | −0.608 | −0.142 |
| $SOF_2/TiO_2$-ZnO | Ti-S:3.084 | −0.402 | 0.083 |
| $SO_2F_2/TiO_2$-ZnO | S-O:3.214 | −0.549 | 0.061 |

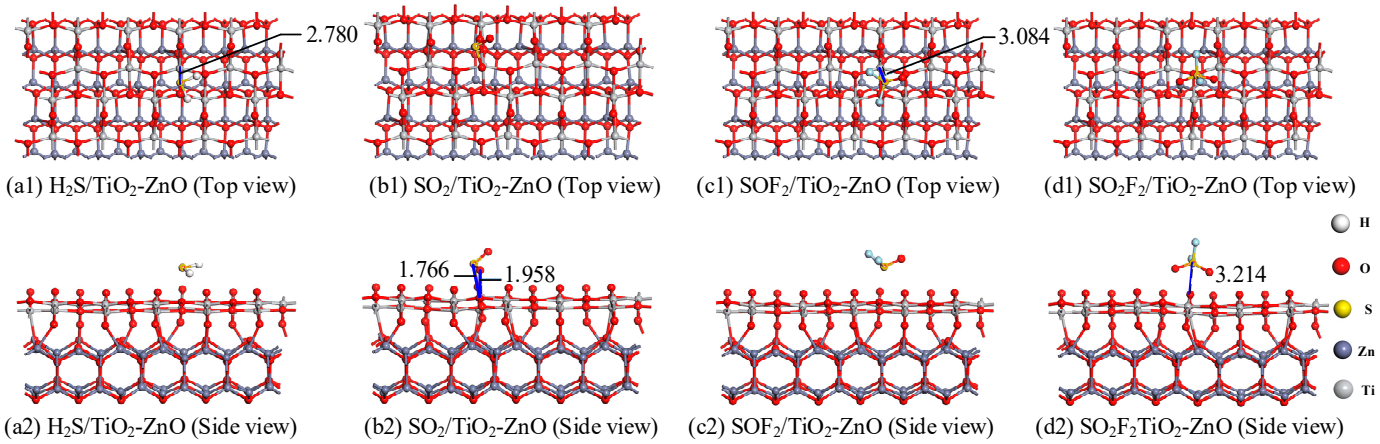



**Figure 7.** The gasses adsorption structures of (**a1**,**a2**) $H_2S$, (**b1**,**b2**) $SO_2$, (**c1**,**c2**) $SOF_2$, and (**d1**,**d2**) $SO_2F_2$ on $TiO_2$-ZnO heterojunction.

- DOS, CDD, and molecular orbital analysis

To investigate the gas-sensing performance of the $TiO_2$-ZnO heterojunction on $H_2S$, $SO_2$, $SOF_2$, and $SO_2F_2$ gas molecules, the density of states distribution of the four gas adsorption systems was analyzed, as shown in Figure 8. There is no significant change in TDOS before and after the four gas molecules' adsorption on the surface of the $TiO_2$-ZnO heterojunction. From PDOS analysis, it can be seen that the degree of atomic orbital hybridization is very weak. Therefore, it is not possible to accurately determine the changes in conductivity from the density of states analysis. Figure 9 shows the distribution of charges upon gas adsorption. From Figure 9a, it can be observed that the electron density around $H_2S$ gas is relatively low, which is consistent with the conclusion that the $H_2S$ molecule acts as an electron donor. In Figure 9b, the blue color is around the S atom of the $SO_2$ gas molecule and the red color is around the O atoms of the $TiO_2$ layer, indicating that $SO_2$ receives electrons from the $TiO_2$ layer. This conclusion stays consistent with the charge transfer of $SO_2$ of $-0.142$ $|e|$ during the adsorption process. In the $SOF_2$ and $SO_2F_2$ adsorption systems, there is no significant change in the distribution of electrons, indicating a small amount of charge transfer.

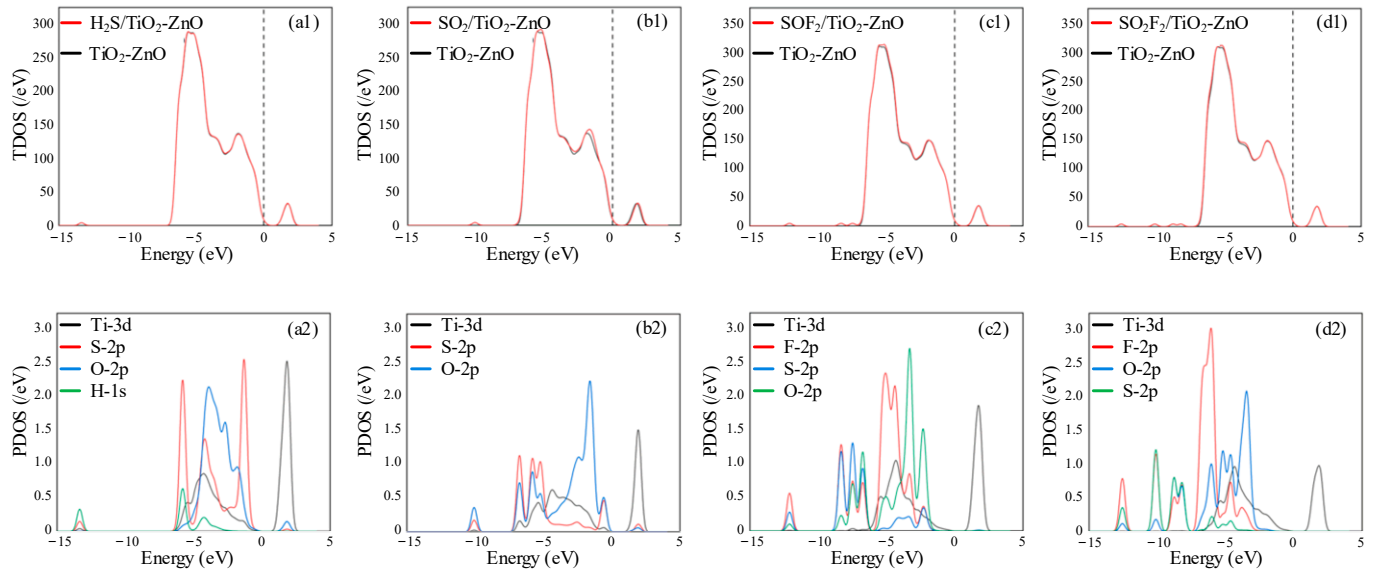



**Figure 8.** The TDOS and PDOS of (**a1**,**a2**) $H_2S$, (**b1**,**b2**) $SO_2$, (**c1**,**c2**) $SOF_2$, and (**d1**,**d2**) $SO_2F_2$ on $TiO_2$-ZnO heterojunction.

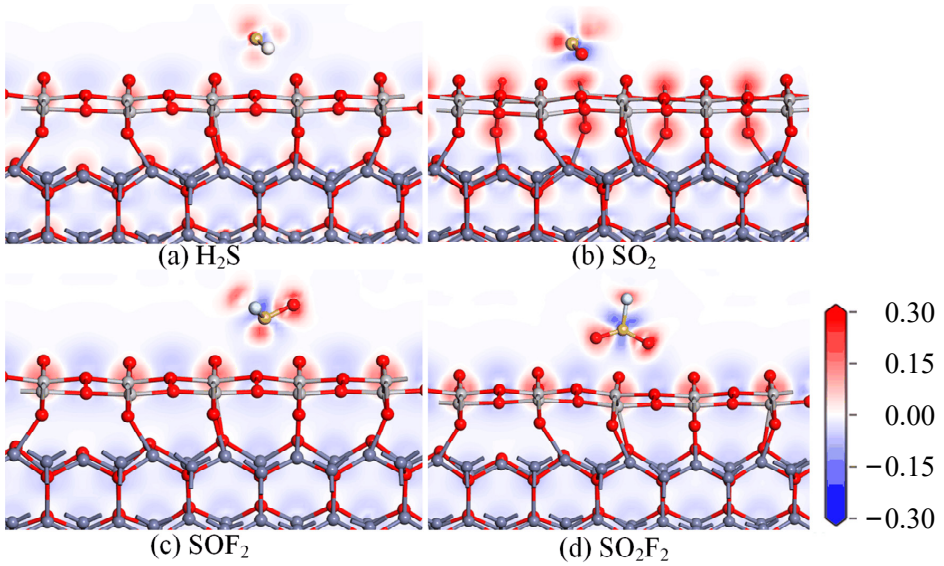



**Figure 9.** The CDD of (**a**) $H_2S$, (**b**) $SO_2$, (**c**) $SOF_2$, and (**d**) $SO_2F_2$ on $TiO_2$-ZnO heterojunction.

Figure 10 shows the frontier molecular orbitals' distribution and the related energy of the gas molecules before and after adsorption on the surface of the $TiO_2$-ZnO heterojunction. Before gas adsorption, LUMO is mainly distributed on the $TiO_2$ layer, while HOMO is mainly distributed on the ZnO heterojunction layer, and both are evenly distributed. The energy corresponding to LUMO is −4.921 eV, and the energy corresponding to HOMO is −6.213 eV. In the three gas adsorption systems of $H_2S$, $SOF_2$, and $SO_2F_2$, the energy gap only undergoes slight changes, within a range of less than 0.03 eV. The conductivity of the $H_2S$ and $SOF_2$ gas adsorption systems increases, while the conductivity of the $SO_2F_2$ gas adsorption systems decreases. In the $SO_2$ gas adsorption system, the distribution of LUMO on the $TiO_2$ layer becomes thinner, followed by a significant increase in the energy gap value, which is 0.086 eV. This means there is a significant increase in conductivity after gas adsorption, providing a theoretical basis for the development of resistive chemical sensors.

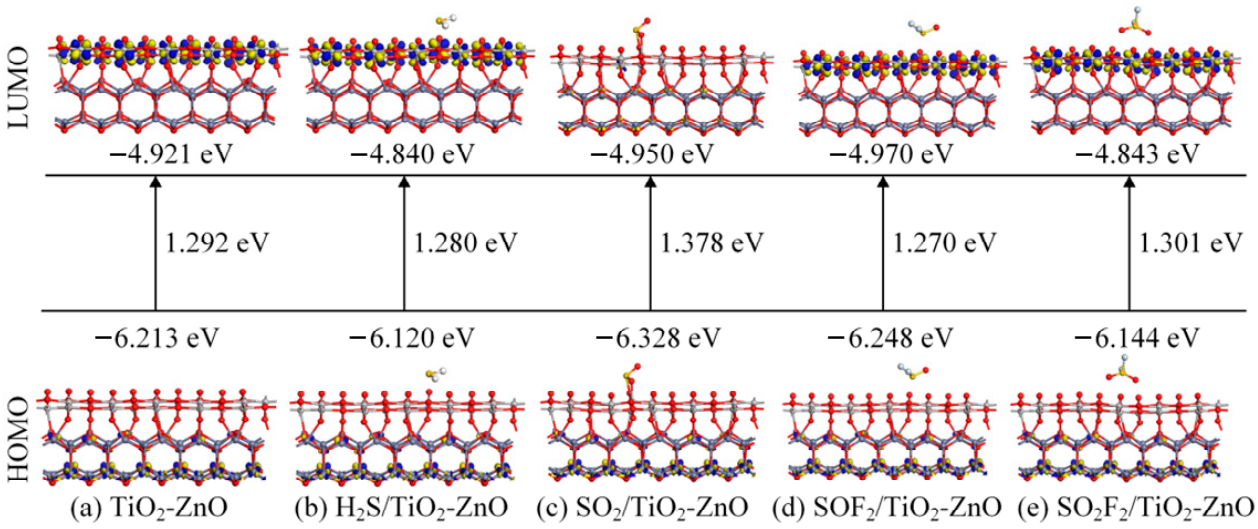



**Figure 10.** Calculated frontier molecular orbitals, HOMO and LUMO, before and after gas adsorption on $TiO_2$-ZnO heterojunction.

This section investigated the gas-sensing response of $TiO_2$-ZnO heterojunctions to four gas molecules. Based on DFT calculations, the most stable heterostructure and gas adsorption model were calculated, and the gas-sensing performance of the $TiO_2$-ZnO heterojunction heterostructure on four gas molecules was explored by analyzing density

of states, CDD, and the HOMO-LUMO gap. The calculation results show that the $TiO_2$ and ZnO crystal planes can form stable heterojunctions with high formation energy. The adsorption type of $H_2S$, $SOF_2$, and $SO_2F_2$ by the $TiO_2$-ZnO heterojunction is physical adsorption, while the adsorption type of $SO_2$ is chemical adsorption. The conductivity of the $TiO_2$-ZnO heterojunction increases after adsorbing $H_2S$ and $SOF_2$ gas molecules; after adsorbing $SO_2$ and $SO_2F_2$, there is a decrease in conductivity. Specifically, the change in conductivity is most significant after the adsorption of $SO_2$, indicating that the $TiO_2$-ZnO heterojunction can effectively detect $SO_2$ gas.

## 3. Methods

All calculations were performed based on DFT [27]. Specifically, the generalized gradient approximation method with a GGA-PBE function was used for geometric optimization and energy calculation [28], while the Tkatchenko–Scheffler method was used to correct the van der Waals force to obtain accurate results [29]. In addition, a DFT semi-core pseudopotential (DSSP) was adopted and its value was set to 6 [30]. The K-points in the Brillouin area were set to $5 \times 5 \times 1$. The energy convergence accuracy, maximum stress, and displacement were set to $2.721 \times 10^{-4}$ eV, 0.109 eV/Å, and 0.005 Å, respectively [31,32]. To eliminate the influence of interlayer interactions, the thickness of the vacuum layer was set to 20 Å.

## 4. Conclusions

In order to achieve the online monitoring of GIS faults, this study analyzed the adsorption and gas-sensing properties of $In_2O_3$-ZnO and $TiO_2$-ZnO heterojunctions on four $SF_6$ decomposition gasses ($H_2S$, $SO_2$, $SOF_2$, and $SO_2F_2$). Compared to intrinsic $In_2O_3$ and ZnO, the band value of the $In_2O_3$-ZnO heterojunction significantly decreases. The energy band value of the $TiO_2$-ZnO heterojunction is larger than that of the $In_2O_3$-ZnO heterojunction. The $In_2O_3$-ZnO heterojunction shows large adsorption energy for $H_2S$ and $SO_2$ via chemical adsorption, and small adsorption energy for $SOF_2$ and $SO_2F_2$ via physical adsorption. After gas adsorption, the conductivity of the $H_2S$ adsorption system increases, while the conductivity of the $SO_2$ adsorption system decreases. The $In_2O_3$-ZnO heterojunction can serve as an adsorbent material for $H_2S$ gas molecules, while it can also be used as a gas-sensitive material for $SO_2$ gas molecules. While $TiO_2$-ZnO only shows chemical adsorption for $SO_2$, there is a distinct change in the conductivity of the adsorption system. The research results play an important role in exploring novel gas-sensitive materials and preparing a specific gas sensor using the online monitoring of power insulation equipment.

**Supplementary Materials:** The following are available online at https://www.mdpi.com/article/10.3390/ijms25158009/s1.

**Author Contributions:** Conceptualization, T.Z.; methodology, Y.G.; software, D.M.; validation, T.Z.; formal analysis, T.Z.; investigation, T.Z.; resources, D.M.; data curation, T.Z.; writing—original draft preparation, T.Z.; writing—review and editing, Y.G.; visualization, Y.G.; supervision, Y.G.; project administration, Y.G.; funding acquisition, T.Z. All authors have read and agreed to the published version of the manuscript.

**Funding:** This research was funded by Talent Introduction Program of Chengdu Normal University (No. YJRC 2020-14), and Innovative Experimental Project of Chengdu Normal University (No. 2023JG09, No. CXSY2024009).

**Institutional Review Board Statement:** Not applicable.

**Informed Consent Statement:** Not applicable.

**Data Availability Statement:** Data are contained within the article and Supplementary Materials.

**Conflicts of Interest:** The authors declare no conflicts of interest.

## Abbreviations

| | |
|---|---|
| $SF_6$ | sulfur hexafluoride |
| GIS | gas insulated switchgear |
| TMDCs | two-dimensional metal sulfur compounds |
| VOCs | volatile organic compounds |
| DFT | density functional theory |
| DOS | density of states |
| TDOS | total density of states |
| PDOS | partial density of states |
| CDD | charge difference density |
| LUMO | lowest unoccupied molecular orbital |
| HOMO | highest occupied molecular orbital |
| GGA | generalized gradient approximation |
| PBE | Perdew–Burke–Ernzerhof |
| DSSP | DFT semi-core pseudopotential |

## References


1. Wang, J.; Chen, W.; Wang, P.; Wan, F.; Zhang, Z.; Gao, S.; Wang, Y. Analysis of SF6 decomposed products by fibre-enhanced Raman spectroscopy for gas-insulated switchgear diagnosis. *High Volt.* **2024**, *9*, 206–216. [CrossRef]
2. Khan, Q.; Refaat, S.S.; Abu-Rub, H.; Toliyat, H.A. Partial discharge detection and diagnosis in gas insulated switchgear: State of the art. *IEEE Electr. Insul. Mag.* **2019**, *35*, 16–33. [CrossRef]
3. Zhuang, Y.; Hu, X.; Tang, B.; Wang, S.; Cui, A.; Hou, K.; He, Y.; Zhu, L.; Li, W.; Chu, J. Effects of SF6 decomposition components and concentrations on the discharge faults and insulation defects in GIS equipment. *Sci. Rep.* **2020**, *10*, 15039. [CrossRef] [PubMed]
4. Faizol, Z.; Zubir, F.; Saman, N.M.; Ahmad, M.H.; Rahim, M.K.A.; Ayop, O.; Jusoh, M.; Majid, H.A.; Yusoff, Z. Detection Method of Partial Discharge on Transformer and Gas-Insulated Switchgear: A Review. *Appl. Sci.* **2023**, *13*, 9605. [CrossRef]
5. Fan, X.; Li, L.; Zhou, Y.; Tang, N.; Zou, Z.; Li, X.; Huang, G.; Liu, M. Online detection technology for SF6 decomposition products in electrical equipment: A review. *IET Sci. Meas. Technol.* **2018**, *12*, 707–711. [CrossRef]
6. Fang, H.; Chen, H.; Zhang, F.; Tan, R.; Han, C.; Ai, X.; Ma, X.; Cui, Y.; Wang, D. Trace detection of SF6 gas decomposition component $H_2S$ based on $Pr_6O_{11}$-$In_2O_3$. *Sens. Actuators B Chem.* **2024**, *412*, 135822. [CrossRef]
7. Li, Z.; Jia, L.; Chen, J.; Cui, X.; Zeng, W.; Zhou, Q. Ag-modified hexagonal GaN monolayer as an innovative gas detector toward SF6 decomposed species: Insights from the first-principles computations. *Appl. Surf. Sci.* **2022**, *589*, 153000. [CrossRef]
8. Wang, L.; Wang, X.; Yan, Y.; Qiu, H.; Guo, X.; Tang, J.; Zeng, F. Theoretical analysis of Ni atom-doped MXene for improving the catalytic degradation performance of SF6. *Comput. Theor. Chem.* **2023**, *1229*, 114325. [CrossRef]
9. Meng, H.; Liu, Z.; Wang, X.; Feng, L. A fluorinated greenhouse gas sensor based on N-doped tin oxide materials. *Environ. Sci.-Nano* **2024**, *11*, 459–469. [CrossRef]
10. Krishna, K.G.; Parne, S.; Pothukanuri, N.; Kathirvelu, V.; Gandi, S.; Joshi, D. Nanostructured metal oxide semiconductor-based gas sensors: A comprehensive review. *Sens. Actuators A Phys.* **2022**, *341*, 113578. [CrossRef]
11. Franco, M.A.; Conti, P.P.; Andre, R.S.; Correa, D.S. A review on chemiresistive ZnO gas sensors. *Sens. Actuators Rep.* **2022**, *4*, 100100. [CrossRef]
12. Yuan, H.; Aljneibi, S.A.A.A.; Yuan, J.; Wang, Y.; Liu, H.; Fang, J.; Tang, C.; Yan, X.; Cai, H.; Gu, Y.; et al. ZnO Nanosheets Abundant in Oxygen Vacancies Derived from Metal-Organic Frameworks for ppb-Level Gas Sensing. *Adv. Mater.* **2019**, *31*, 1807161. [CrossRef] [PubMed]
13. Alenezi, M.R. Hierarchical zinc oxide nanorings with superior sensing properties. *Mater. Sci. Eng. B* **2018**, *236–237*, 132–138. [CrossRef]
14. Zhao, S.; Shen, Y.; Li, A.; Chen, Y.; Gao, S.; Liu, W.; Wei, D. Effects of rare earth elements doping on gas sensing properties of ZnO nanowires. *Ceram. Int.* **2021**, *47*, 24218–24226. [CrossRef]
15. Zhang, B.; Sun, J.-Y.; Gao, P.-X. Low-Concentration NOx Gas Analysis Using Single Bimodular ZnO Nanorod Sensor. *ACS Sens.* **2021**, *6*, 2979–2987. [CrossRef] [PubMed]
16. Razavi, R.; Nejad, F.G.; Ahmadi, S.A.; Beitollahi, H. Synthesis of ZnO@$TiO_2$ nanoparticles and its application to construct an electrochemical sensor for determination of hydrazine. *Electrochem. Commun.* **2024**, *159*, 107639. [CrossRef]
17. Tian, X.; Cui, X.; Lai, T.; Ren, J.; Yang, Z.; Xiao, M.; Wang, B.; Xiao, X.; Wang, Y. Gas sensors based on $TiO_2$ nanostructured materials for the detection of hazardous gases: A review. *Nano Mater. Sci.* **2021**, *3*, 390–403. [CrossRef]
18. Haidry, A.A.; Xie, L.; Wang, Z.; Zavabeti, A.; Li, Z.; Plecenik, T.; Gregor, M.; Roch, T.; Plecenik, A. Remarkable Improvement in Hydrogen Sensing Characteristics with Pt/TiO2 Interface Control. *ACS Sens.* **2019**, *4*, 2997–3006. [CrossRef] [PubMed]
19. Tshabalala, Z.P.; Swart, H.C.; Motaung, D.E. Fabrication of TiO2 nanofibers based sensors for enhanced CH4 performance induced by notable surface area and acid treatment. *Vacuum* **2021**, *187*, 110102. [CrossRef]
20. Shooshtari, M.; Salehi, A. An electronic nose based on carbon nanotube-titanium dioxide hybrid nanostructures for detection and discrimination of volatile organic compounds. *Sens. Actuators B-Chem.* **2022**, *357*. [CrossRef]

21. Shah, S.; Hussain, S.; Din, S.T.U.; Shahid, A.; Amu-Darko, J.N.O.; Wang, M.; Tianyan, Y.; Liu, G.; Qiao, G. A review on $In_2O_3$ nanostructures for gas sensing applications. *J. Environ. Chem. Eng.* **2024**, *12*, 112538. [CrossRef]
22. Sui, N.; Zhang, P.; Zhou, T.; Zhang, T. Selective ppb-level ozone gas sensor based on hierarchical branch-like $In_2O_3$ nanostructure. *Sens. Actuators B Chem.* **2021**, *336*, 129612. [CrossRef]
23. Liang, X.; Zhang, J.; Du, L.; Zhang, M. Effect of resonant tunneling modulation on ZnO/In2O3 heterojunction nanocomposite in efficient detection of NO2 gas at room temperature. *Sens. Actuators B Chem.* **2021**, *329*, 129230. [CrossRef]
24. Yang, S.; Lei, G.; Xu, H.; Lan, Z.; Wang, Z.; Gu, H. Metal Oxide Based Heterojunctions for Gas Sensors: A Review. *Nanomaterials* **2021**, *11*, 1026. [CrossRef] [PubMed]
25. Gai, L.-Y.; Lai, R.-P.; Dong, X.-H.; Wu, X.; Luan, Q.-T.; Wang, J.; Lin, H.-F.; Ding, W.-H.; Wu, G.-L.; Xie, W.-F. Recent advances in ethanol gas sensors based on metal oxide semiconductor heterojunctions. *Rare Met.* **2022**, *41*, 1818–1842. [CrossRef]
26. Cheng, C.; Chen, C.; Zhang, H.; Zhang, Y. Preparation and study of ammonia gas sensor based on ZnO/CuO heterojunction with high performance at room temperature. *Mater. Sci. Semicond. Process.* **2022**, *146*, 106700. [CrossRef]
27. Zoromba, M.S.; Alharbi, F.; Al-Hossainy, A.F.; Abdel-Aziz, M.H. Preparation of hybrid conducting polymers blend nanocomposite for energy conversion using experimental data and TD-DFT/DMOl3 computations. *J. Mater. Res. Technol.* **2023**, *23*, 2852–2867. [CrossRef]
28. Haas, P.; Tran, F.; Blaha, P. Calculation of the lattice constant of solids with semilocal functionals. *Phys. Rev. B* **2009**, *79*, 085104. [CrossRef]
29. Bučko, T.; Lebègue, S.; Hafner, J.; Ángyán, J.G. Tkatchenko-Scheffler van der Waals correction method with and without self-consistent screening applied to solids. *Phys. Rev. B* **2013**, *87*, 064110. [CrossRef]
30. Muvva, C.; Murugan, N.A.; Subramanian, V. Assessment of Amyloid Forming Tendency of Peptide Sequences from Amyloid Beta and Tau Proteins Using Force-Field, Semi-Empirical, and Density Functional Theory Calculations. *Int. J. Mol. Sci.* **2021**, *22*, 3244. [CrossRef]
31. Gui, Y.; Lin, Y.; Ji, C.; Luo, P.; Chen, X. Density Functional Theory Calculations for the Adsorption Property of Hazardous Industrial Gasses on Transition-Metal-Modified MoS2 Nanosheets. *ACS Appl. Nano Mater.* **2022**, *5*, 11111–11118. [CrossRef]
32. Wang, Y.; Gui, Y.; Ji, C.; Tang, C.; Zhou, Q.; Li, J.; Zhang, X. Adsorption of $SF_6$ decomposition components on $Pt_3$-$TiO_2$(1 0 1) surface: A DFT study. *Appl. Surf. Sci.* **2018**, *459*, 242–248. [CrossRef]


**Disclaimer/Publisher's Note:** The statements, opinions and data contained in all publications are solely those of the individual author(s) and contributor(s) and not of MDPI and/or the editor(s). MDPI and/or the editor(s) disclaim responsibility for any injury to people or property resulting from any ideas, methods, instructions or products referred to in the content.